Available online at www.sciencedirect.com
SCIENCE DIRECT
Physics of the Earth and Planetary Interiors 155 (2006) 236–248
PHYSICS OF THE EARTH AND PLANETARY INTERIORS
www.elsevier.com/locate/pepi

Tomographic investigation of the wear along the San Jacinto fault, southern California

Tae-Kyung Hong *, William Menke

Lamont-Doherty Earth Observatory of Columbia University, 61 Route 9W, Palisades, NY 10964, USA

Received 25 October 2005; received in revised form 14 December 2005; accepted 19 December 2005

Abstract

The seismic properties of the wear along the San Jacinto fault are investigated using local seismic records for clustered fault-zone earthquakes. Spatial reciprocity allows us to use the seismicity along fault plane to mimic the situation where receiver arrays are placed at depth on the fault plane. A seismic record at the event location is constructed by stacking the original station records. Waveform cross-correlations is then used to calculate the traveltimes of shear waves traveling between the pair of events. We analyze 157 small earthquakes occurring between 1998 and 2004 on the San Jacinto and Elsinore fault zones. Low shear velocities in the San Jacinto fault zone related to wear and gouge are persistently observed up to the depth of brittle–ductile transition zone (∼16 km). On the other hand, low velocities in the Elsinore fault zone are only visible in the northwestern portion at shallow depth. The wear structures in the San Jacinto fault zone display lower shear velocities by 6–8% than those of the wall-rock.

Keywords: Wear; Cross-correlation; Shear-wave structure; Brittle–ductile transition zone; Southern California; San Jacinto; Elsinore; Fault zone

1. Introduction

The seismic structures of fault zones have been studied to understand the earthquake physics and to mitigate seismic hazard. Seismic structure reflects the physical and chemical conditions of the medium, and these conditions are directly related to the fault strength. The depth extent of the low seismic velocities within the fault zone is especially important because it relates the key fault properties such as rheology, brittle–ductile transition, pore pressure, stress, geotherm, and rupture energy. Resolving the seismic structure along fault zone provides insight into the nature of fault zone.

The narrow width of the zone of wear on fault plane, which typically ranges from tens to hundreds meters, makes applying conventional tomography techniques difficult, because such studies normally analyze phases with much longer wavelengths (e.g., Scott et al., 1994; Kohler et al., 2003). One approach to studying the wear is to analyze high-frequency trapped waves, which are guided in the low-velocity structure (Li et al., 1997; Mizuno et al., 2004; Lewis et al., 2005). This method determines fault-zone model parameters (e.g., fault-zone width, velocity, Q, wall-rock velocity, depth extent of structure) by least-square matching of observed and synthetic seismograms. The model parameters trade off each other, and the scheme suffers from nonuniqueness (Li

* Corresponding author. Tel.: +1 845 365 8944; fax: +1 845 365 8150.
E-mail address: tkhong@ldeo.columbia.edu (T.-K. Hong).

0031-9201/$ – see front matter © 2005 Elsevier B.V. All rights reserved.
doi:10.1016/j.pepi.2005.12.005

et al., 2002), although the nonuniqueness can be partially improved with parameters from other available resources.

Further, choice of starting model has a major impact on the solution in this model-based inversion approach. For instance, in a study of the San Jacinto fault zone, Li and Vernon (2001) implemented a base model in which seismic velocity increases gradually with depth. Their resulting model has a gradual low-velocity zone extending to a depth of 15–20 km. On the other hand, for the same fault zone, Lewis et al. (2005) performed an inversion based on a homogeneous-layer model and argued that a homogeneous low-velocity structure extends only up to 3–5 km. The trapped-wave technique requires local array recording across the fault trace for the analysis. The trapped waves are recorded large at stations near the fault plane, and decreases with distance from the fault plane (Li et al., 1997; Hong and Kennett, 2003). This requirement of near-fault-trace observations limits the applicability of the technique.

Inverse techniques that do not require starting models and use more broad broadly scattered stations, such as those of existing earthquake monitoring networks, are desirable for the investigation of fault-zone structure. A key requirement of such a technique is the ability to estimate seismic traveltimes along paths entirely confined to the fault zone. In this study, we utilize a spatial reciprocity principle (Aki and Richards, 1980), which allows us to use fault-zone earthquakes to simulate the situation where dense arrays of seismometers are deployed in the fault plane.

Recently, seismograms of dispersive surface waves, traveling between two stations, have been constructed from cross-correlation of seismic noise records. The inter-station surface-wave traveltimes were used to construct 1D shear-wave profiles of the inter-station regions (Shapiro and Campillo, 2004; Shapiro et al., 2005). The technique relies on the natural tendency of scattering from small heterogeneities in earth structure to create seismic waves traveling in all possible directions. The wavefield is diffusive, with a spatially homogeneous energy distribution. Cross-correlation is used to select just one of these waves, the one traveling from one specified station to another, yielding the Green's function between the stations. Seismic coda can be used as an alternative to seismic noise (Campillo and Paul, 2003; Paul et al., 2005).

In this study, we extend the cross-correlation technique using the principle of spatial reciprocity, which allows us to reconstruct waves traveling between pairs of events. Since small earthquakes are normally clustered on the rupture plane, the reconstructed wavefield can be used to estimate traveltimes of waves between pairs of events, both of which are located deep on the fault plane. The estimated velocities reflect the seismic properties of the wear on the fault plane. We apply the method to the events around the San Jacinto fault zone, which is one of most active seismogenic regions in southern California. We examine the shear-wave velocities in the fault zones, the depth extent of the low-velocity wear in the fault zone, and the implication to physical properties.

2. Method

The seismic reciprocity theorem (Aki and Richards, 1980, p. 28) states that the source and receiver can be exchanged without affecting the observed seis-mogram. Thus, for instance, the Green's function, tensor G obeys the rule:

$$G_{ij}(x_1, t; x_2, 0) = G_{ji}(x_2, t; x_1, 0). \quad (1)$$

Here $G_{ij}(x_1, t; x_2, 0)$ represents the ith-component displacement at location x_1 and time t for a unit impulse in the j direction at a location of x_2. The reciprocity theorem works not only for unidirectional force, but also for dislocation sources like earthquakes (Spudich and Bostwick, 1987) and explosion sources (Nowack and Chen, 1999). Under the reciprocity theorem, the i-component seismogram at a surface receiver for a dislocation at depth corresponds to a traction seismogram at the source location for an i-directional impulse on the station location (Spudich and Bostwick, 1987). Thus, seismic records for an event at individual stations can be treated as observations at the event location for synchronized sources at the station locations. The property of the reciprocity has been widely utilized in array analyses of source properties, geological and tectonic structures, and phase composition of waves (Spudich and Bostwick, 1987; Scherbaum et al., 1991; Xie et al., 1996; Hong and Xie, 2005; Hong and Menke, submitted for publication).

Using this reciprocity principle, we construct a scenario in which a receiver is surrounded by multiple sources with uniform source parameters, which are synchronized by the event origin time. We obtain a time record at the event location for the synchronized multiple sources at the station locations. Waves, $s_{ij}(t)$, traveling from a source i to a station j, can be expressed by:

$$s_{ij}(t) = \sum_{k=1}^{M} a_k r_{ij}^k(t). \quad (2)$$

Here a_k is the amplitude of ray r_{ij}^k, which travels along a path of k from source i to station j; and M the number of all ray paths between the source and the receiver including

multi-scattering ray paths. The time t is the lapse time after event origin time. Thus, the seismogram, $n_i(t)$, at event location i, can be can be obtained by adding all records. In order to equalize the influence of each record, $s_{ij}(t)$, we normalize every record:

$$n_i(t) = \sum_{j=1}^{N} \frac{1}{A_{ij}} s_{ij}(t). \tag{3}$$

Here A_{ij} is the maximum amplitude of record s_{ij}; and N the number of stations.

The ensemble seismogram, $n_i(t)$, represents the signal that would be observed by a "virtual" receiver, if it were placed at the location of the actual source, i, and recorded many "virtual" events ($j = 1, 2, \ldots, N$) which activated simultaneously at the actual station locations. The amplitude of each of these virtual events has been adjusted through the normalization factor, A_{ij}, to cause similar amplitude signals at the virtual station. The normalization approximately corrects the amplitude of the most prominent phase for geometrical spreading. The ensemble seismogram, $n_i(t)$, is for many simultaneous but geographically-distributed virtual sources. Furthermore, each virtual source generates various scattered waves. Thus, the corresponding "virtual wavefield" contains wave passing through every point, and traveling in every direction. Owing to the azimuthal distribution of stations to the events (Fig. 1), the constructed ensemble wavefield is quasi-diffusive. An example of original and stacked seismograms for the San Jacinto fault zone is shown in Fig. 2.

Campillo and Paul's (2003) and Shapiro et al.'s (2005) approach, which is suitable for seismic noise and coda, introduces a process of one-bit signal stacking which disregards the amplitude of each wavelet. Their approach accounts for the facts that each noise source is non-uniform in strength and the amplitude of scattered seismic coda decreases exponentially with time. In this study, all records originate from the same source and can be analyzed with a common weight, allowing us to utilize full dynamic-range waveforms in the cross-correlation analysis. As a result, this process allows us to incorporate micro-earthquakes that can not produce strong coda. Since we use data from stations that surround the events on the fault, the virtual wave field is being generated by well-distributed sources and becomes diffusive (Paul et al., 2005).

The traveltime between two events, i and j, is obtained by cross-correlating the ensemble signals $n_i(t)$ and $n_j(t)$:

$$C_{ij}(\tau) = \frac{1}{N_i N_j} \int n_i(t)\, n_j(t+\tau)\, \mathrm{d}t, \tag{4}$$

where N_i is given by

$$N_i = \sqrt{\int n_i^2(t)\, \mathrm{d}t}. \tag{5}$$

The key idea is that waves observed on the two virtual stations are incoherent except for the special case of a wave that originates at a place in an extrapolated great-circle path of virtual stations and propagates along the great-circle path between them. The maximum amplitude of the cross-correlation coefficient C_{ij} is measured for waves traveling on this path (e.g., direct waves recorded at stations of filled triangles in Fig. 1). On the other hand, waves propagating along other paths are de-correlated (the stations marked with open triangles in the figure). Waves traveling along the great-circle, but originating between the virtual stations, produce an oscillatory behavior in cross-correlation, and also de-correlate (Snieder, 2004). The cross-correlation process thus records the Green's function for propagation between the pair of virtual stations. The Green's function can be retrieved even when the virtual events are distributed inhomogeneously (Paul et al., 2005).

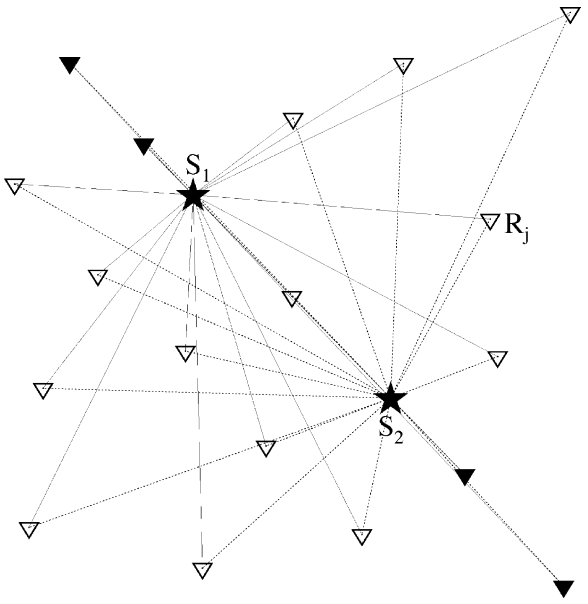

Fig. 1. Schematic diagram of a pair of events (S_1, S_2) and a group of recording stations (R_j, $j = 1,2, \ldots, N$, where N is the number of receivers). The great-circle paths from events to stations are marked with lines. Under the reciprocity theorem, records at event locations for synchronized impulses at the surrounding station locations can be constructed by stacking the records of stations. The waves (marked with filled triangles) at receivers located in the extensional part of the great-circle path between two events contribute the construction of correlated phases. A waveform cross-correlation between the stacked records yields the traveltimes of waves propagating between the events.

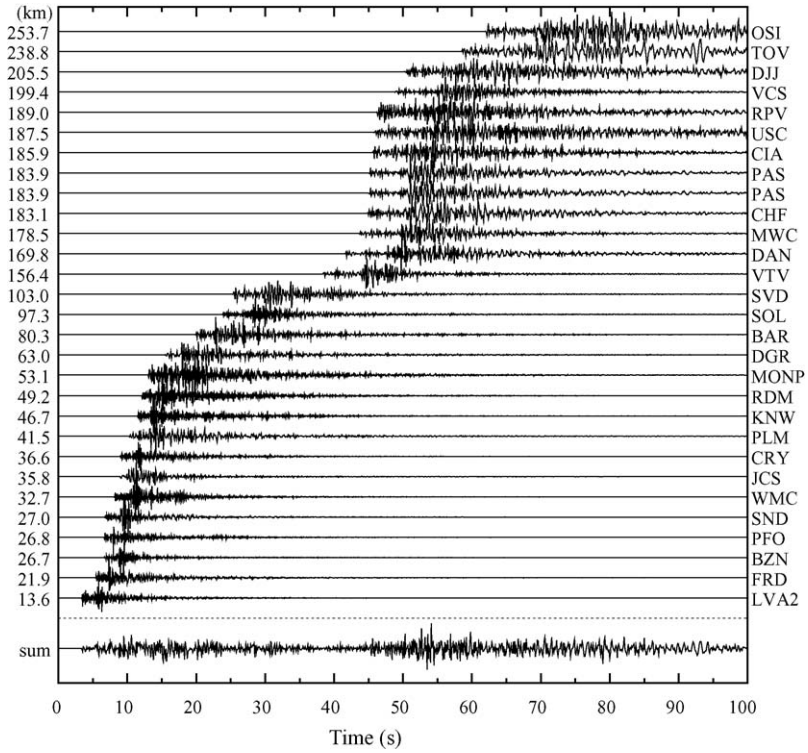

Fig. 2. Construction of an ensemble seismogram at an event location for synchronized impulses at station locations by stacking of records at stations. Leading, compressional wave portion is removed by tapering from every normalized record before stacking, leaving subsequent shear wave portion. The station names are annotated in the right margin, and the distances to the stations are marked in the left margin.

In layered elastic media, various ray paths exist along the great-circle direction. As, however, rays attenuate with propagation distance and time due to geometrical spreading and energy partition at layer boundaries. The delay time of the maximum cross-correlation coefficient is expected to reflect the traveltime of waves along the shortest path between events (i.e., the direct path). Thus, the average velocity (v_{ij}) between two events i and j can be estimated as:

$$v_{ij} = \frac{d_{ij}}{\tau_{ij}}, \tag{6}$$

where τ_{ij} is the delay time of the maximum cross-correlation coefficient; and d_{ij} the distance between the events.

3. Data and geology

We analyze 157 small earthquakes at the San Jacinto and Elsinore fault zones, southern California. These events occurred in a time period of 1998–2004 at a region of latitudes between 32.90 and 33.50° and longitudes between 116.97 and 116.00° (Fig. 3). The events had magnitudes between 2.3 and 4.3, and focal depths between 1 and 20 km. Broadband seismograms of stations, that are placed in a region of latitudes between 32.42 and 35.0° and longitudes between 118.94 and 115.14°, are obtained from the Incorporated Research Institutions for Seismology's Data Management Center (IRIS DMC). We select records with a signal-to-noise ratio of 1.5 or higher. Every event is recorded at between 10 and 75 stations, with a total of 4600 three-component seismograms being used. The source parameters of the events (e.g., epicentral locations, focal depths, origin times and magnitudes) are obtained from the earthquake catalogs of the Southern California Earthquake Center (SCEC) and the National Earthquake Information Center (NEIC).

The San Jacinto fault zone is one of most active seismogenic zone in southern California. Ten earthquakes of magnitude 6 or larger are believed to have occurred since 1890 (Sanders and Kanamori, 1984; Li et al., 1997). The most recent rupture in the San Jacinto fault zone was the $M = 6.5$ Borrego Mountain earthquake of April 9, 1968. Micro-earthquakes reveal that the northwest and southeast portions of the San Jacinto fault zone are seismically

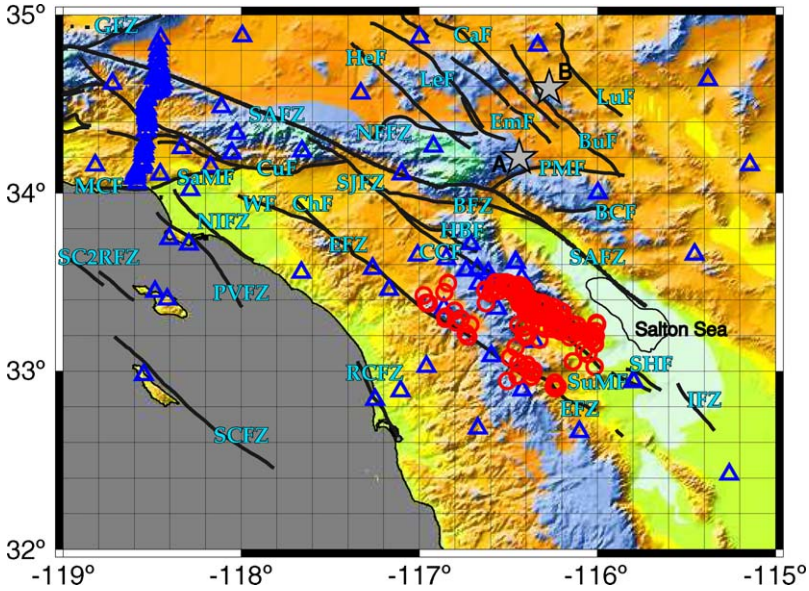

Fig. 3. A map of 157 events (marked with circles) and 124 broad-band stations (triangles) used in this study. Major faults in the area (Jennings, 1994) are marked with solid lines, and their abbreviated names are annotated (BCF: Blue Cut Fault, BFZ: Banning Fault Zone, BuF: Bullion Fault, CaF: Calico Fault, CCF: Coyote Creek Fault, ChF: Chino Fault, CuF: Cucamonga Fault, EFZ: Elsinore Fault Zone, EmF: Emerson Fault, GFZ: Garlock Fault Zone, HBF: Hot Springs and Buck Ridge Faults, HeF: Helendale Fault, IFZ: Imperial Fault Zone, LeF: Lenwood Fault, LuF: Ludlow Fault, MCF: Malibu Coast Fault, NFFZ: North Frontal Fault Zone, NIFZ: Newport-Inglewood Fault Zone, PMF: Printo Mountain Fault, PVFZ: Palos Verdes Fault Zone, RCFZ: Rose Canyon Fault Zone, SAFZ: San Andreas Fault Zone, SaMF: Santa Monica Fault, SCFZ: San Clemente Fault Zone, SC2RFZ: Santa Cruz-Santa Catalina Ridge Fault Zone, SHF: Superstition Hills Fault, SJFZ: San Jacinto Fault Zone, SuMF: Superstition Mountain Fault, WF: Whittier Fault). Two major earthquakes at Landers (1992, M7.3, A) and Hector Mine (1999, M7.2, B) are marked with gray stars.

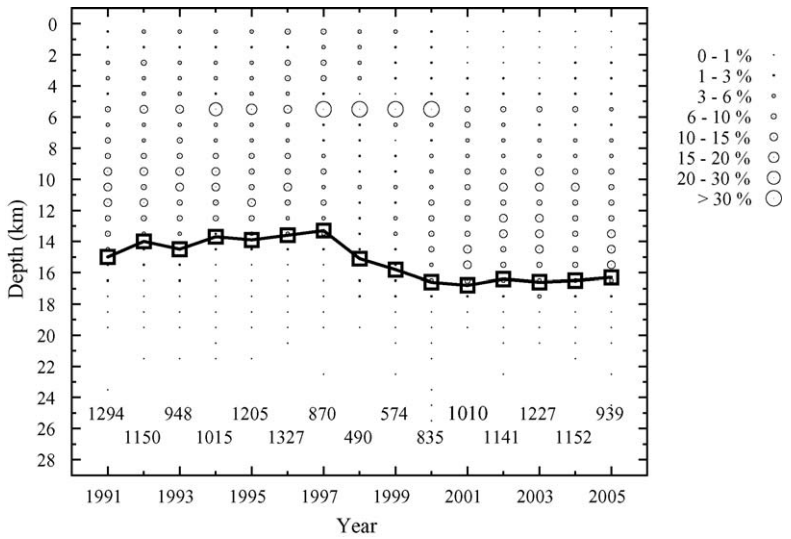

Fig. 4. Focal depth distribution of all seismic events of 1991–2005. The yearly seismicity (number of reported events, N_t) is annotated in the bottom. The number density of events at every 1-km depth ($=N_h/N_t$, where N_h is the number of events at a depth of h) is presented. The depths above which 95% of events are placed (h_{95}) are marked with squares and linked with a solid line. The h_{95} is estimated around 15–16 km.

active. A 20-km long aseismic segment, the Anza gap, intervenes between the active seismic zones (Sanders and Kanamori, 1984).

The most recent major earthquake on the Elsinore fault was a $M = 6.0$ event on May 15, 1910. Historically, this fault zone has been seismically less active than the San Jacinto fault zone. The seismicity in the Elsinore fault zone displays a diffuse pattern with several localized clusters of earthquakes. The seismogenic area of the southeast portion is wider than that of the northwest portion (Magistrale and Rockwell, 1996). Three structural blocks separated by the San Jacinto and Elsinore fault zones are, from west to east, the Santa Ana block (west of the Elsinore fault zone), Perris block (in between the Elsinore and San Jacinto fault zones) and San Jacinto block (east of the San Jacinto fault zone), respectively (Kennedy and Morton, 2003). Recent nearby great earthquakes, occurring on other major faults include Landers (1992, $M = 7.3$) and Hector Mine (1999, $M = 7.2$) (filled stars in Fig. 3).

The depth, h_{95}, above which 95% of earthquakes occur was investigated using hypocentral data from the 1991 to 2005 period (Fig. 4). The parameter h_{95} quantifies the depth of the seismic-aseismic transition (Magistrale, 2002; Rolandone et al., 2004), and is 15–16 km in the study region. Physically, this depth corresponds to the brittle–ductile transition zone which separates the upper frictional and lower plastic deformation regimes (Sibson, 1984; Marone and Scholz, 1988; Scholz, 1998). Our estimate agrees with previous observations (Sanders and Kanamori, 1984; Nazareth and Hauksson, 2004; Hauksson and Shearer, 2005).

Both San Jacinto and Elsinore fault zones are elements of the San Andreas fault system and show right-lateral strike-slip offset. The relative slip rates are 22 mm/year for the San Andreas fault zone, 12 mm/year for the San Jacinto fault zone, and 4–5 mm/year for the Elsinore fault zone (Sanders and Kanamori, 1984; Walls et al., 1998; Grant and Shearer, 2004). The heat flow in the San Jacinto fault zone varies between 60 and 100 mW/m^2, and that in the Elsinore fault zone ranges between 40 and 80 mW/m^2 (Bonner et al., 2003). The heat flow in the northwest portion of the San Jacinto fault zone is lower than that in the southeast portion, with a minimum at around latitude 33.5°. The middle portion of the Elsinore fault zone around 33.2° has lower heat flows than the both northern and southern ends. The focal depth distribution appears to be well correlated with the geothermal variation, with h_{95} corresponding to the 400 °C isotherm (Magistrale, 2002; Bonner et al., 2003).

4. Procedure

The instrument response is removed from each seismogram, and it is bandpass filtered from 0.1 to 8.0 Hz. Shear waves are the highest amplitude part of a local seismogram owing to strong source excitation and dominant shear-to-shear scattering (Aki and Chouet, 1975; Hong, 2004; Hong and Menke, submitted for publication). On the other hand, *P* coda are composed of both compressional and shear scattered waves. In order to estimate shear-wave properties, we remove the *P* and *P* coda portion of each seismogram by tapering to zero of portions corresponding to group velocities of 4.1 km/s and higher. Record sections are normalized and aligned to the event origin time. All records are then stacked to produce a ensemble record according to Eq. (3), which corresponds to an observation at the event location for synchronized impulses at the station locations (Fig. 2). Each component (i.e., Z, N, E) is stacked separately.

For each pair of events, the horizontal-component records are rotated to radial (R) and tangential (T) components, where the sense of R and T is given by the great-circle direction connecting between the two events (Fig. 5). We then cross-correlate all possible combinations of components for the pair of events, and obtain a set of 9 correlograms (R-R, R-T, R-Z, . . ., Z-Z) (Fig. 5). The 9 correlograms correspond to a set of 2D representations of the Green's function, and includes the effect of anisotropy in medium (Paul et al., 2005).

Cross-correlation is used to estimate the traveltime between pairs of events. These traveltimes are then tomographically inverted. We smooth the resulting shear-velocity image over a circular area with a radius of 5 km in order to complement the regions with low paths coverage. As events in fault zone are normally placed on the rupture plane and distributed along the fault trace, the waveform cross-correlation yields the traveltime between events, which is directly related with the wear on the fault plane.

5. Validation and stability

In our method, the delay time of the maximum cross-correlation coefficient is used as an estimate of the traveltime of the direct wave between the events. We test the validity of this approximation using two pairs of events (Fig. 5). The first pair consists of two events separated by a distance of 0.37 km. Its correlograms have a clear maximum at a delay time of 0.1 s. The second pair is separated by 52.1 km. The correlograms show stable and consistent

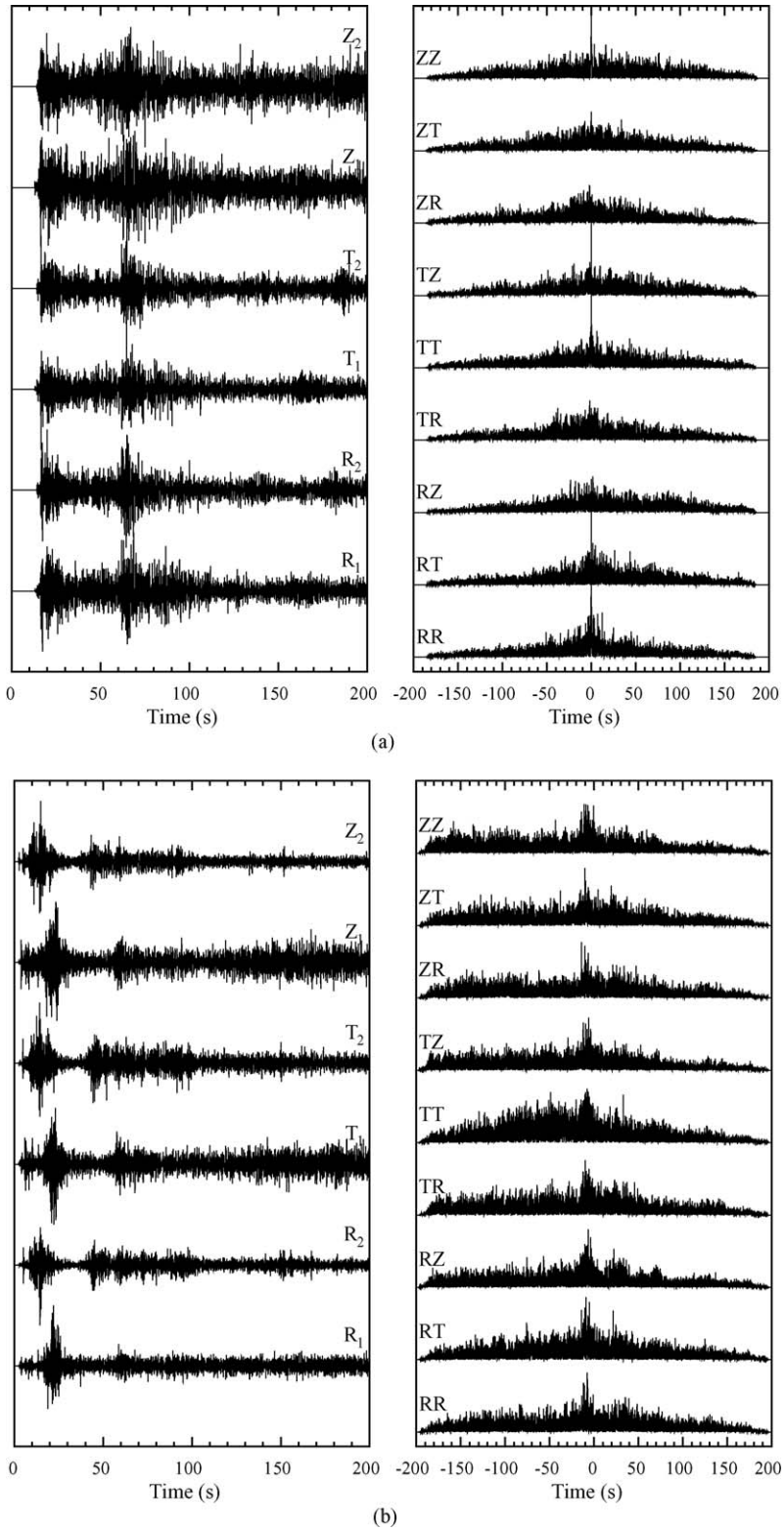

Fig. 5. Constructed three-component (Z, R, T) stacked records of two pairs of events, and the cross-correlations between the stacked records at various combinations of components. The distances between events are: (a) 0.37 km; and (b) 52.1 km. The cross-correlation presents stable and consistent results throughout various sets. The estimated delay times are 0.1 s for (a) and 14.5 s for (b).

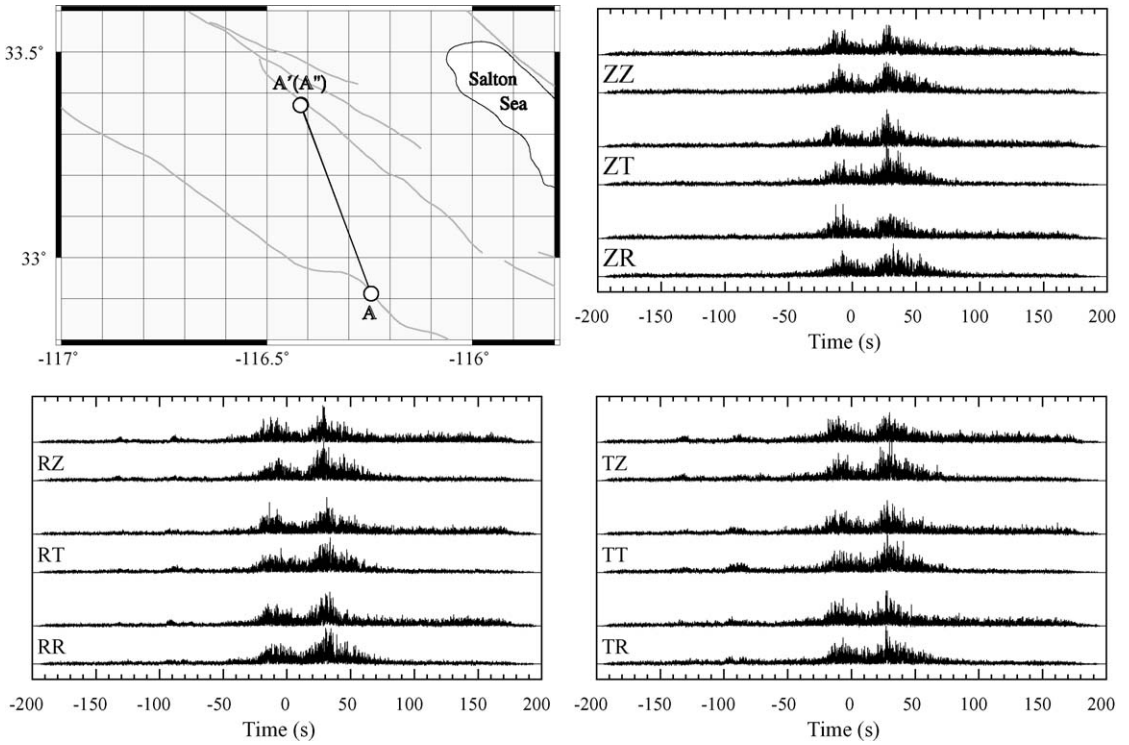

Fig. 6. Comparisons of cross-correlation results between multiple events (A′, A″) with separation of 0.58 km. The distance from the doublet events to a reference event (A) is around 53.6 km. The locations of events are marked on the map. The cross-correlation results are consistent and stable between the doublet events.

variation with a maximum at a delay of 14.5 s. The delay time appears to increase with offset in the expected way.

We now test whether the method provides a consistent estimation between different pairs of events that share the same great-circle path. We use an event doublet (0.58 km spacing) plus a third event located 53.6 km away from them to form to pairs with very similar paths (Fig. 6). Both the two correlograms and the delays estimated from them, are very similar.

We test the stability of the tomographic inversion by comparing the results among various pairs of components (Fig. 7). The tomographic inversion is applied to a data set that is composed of 43 events between 1998 and 2004 with focal depths confined between 13 and 16 km. The estimated velocity structures are coherent and stable, except that slight velocity differences occur at places with low ray coverage. In particular, the San Jacinto fault zone is well resolved throughout all sets of results due to dense population of event pairs along the fault trace. Hereafter we show the average shear-wave structure instead of presenting the 9 sets of results.

6. Results

In order to search for temporal variations in fault zone, we compare the tomographic results between two different time-period data sets: January 1998 to February 2000, and March 2000 to December 2003. Each data set is composed of 52 events, all with magnitudes greater than 2.3 and focal depths between 1 and 20 km (Fig. 8). The average depths, h_{avg}, of the two sets are 8.6 and 10.6 km, and the depths above which 95% of events are placed (h_{95}) are estimated by 16.4 and 15.2 km. The h_{95} of these moderate-size events appear to be close to estimates based on smaller-magnitude data sets (Fig. 4). Differences in the event distribution limit the utility of direct comparisons between images, because the estimated velocities represent different depth-average properties. However, consistency between well-resolved features on vertically extended structures builds confidence in the method.

Shear-wave images from the two time periods are compared in Fig. 9. Both images show a clear low-velocity structure along the San Jacinto fault zone. In contrast, no low-velocity structures are observed along

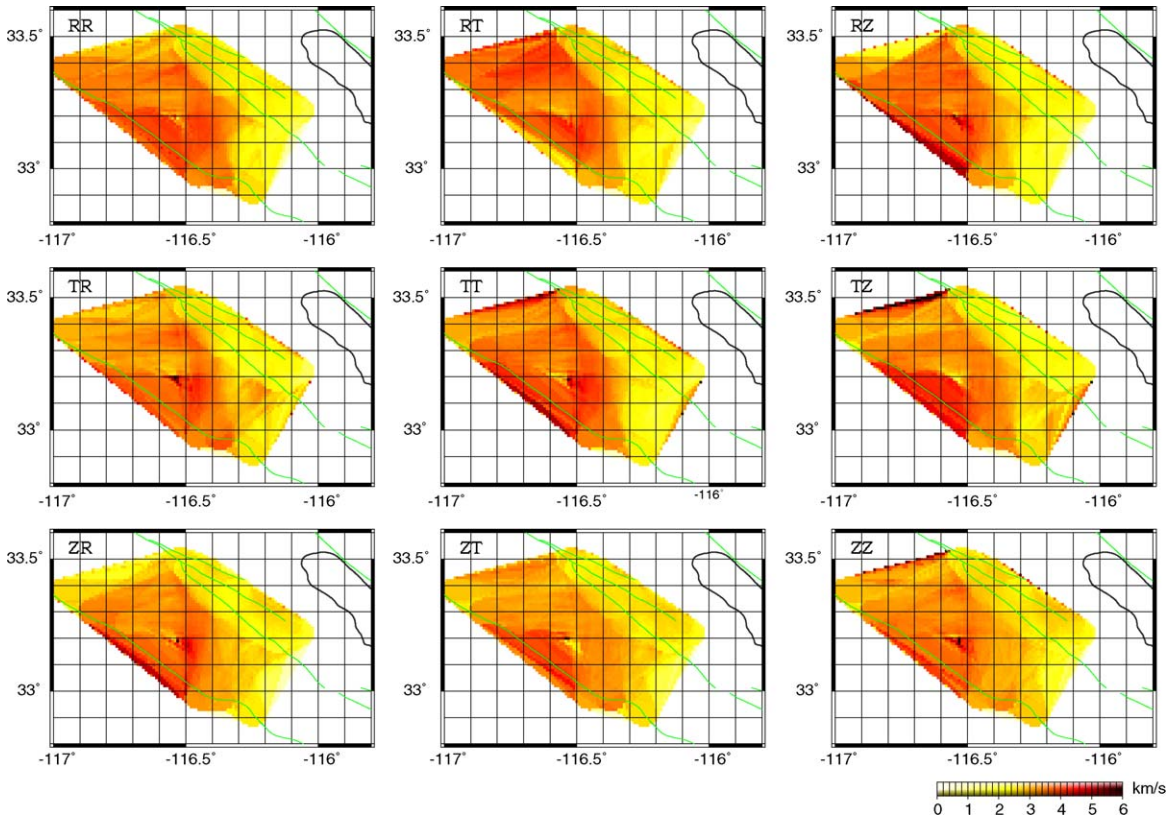

Fig. 7. Tomographic results at various combinations of components for 43 events with depths between 13 and 16 km. The results are consistent over the various sets. A distinct low-velocity structure is observed along the San Jacinto fault zone.

the Elsinore fault zone. Note that the spatial averaging over area with a radius of 5 km has smeared out somewhat. Thus, the fault zones appear wider than their actual width (a couple of hundred meters).

We separately invert data from three depth zones of 6–10 km (34 events), 10–13 km (41 events) and 13–16 km (39 events). The three resulting shear-wave images are presented in Fig. 10. The shear velocity of

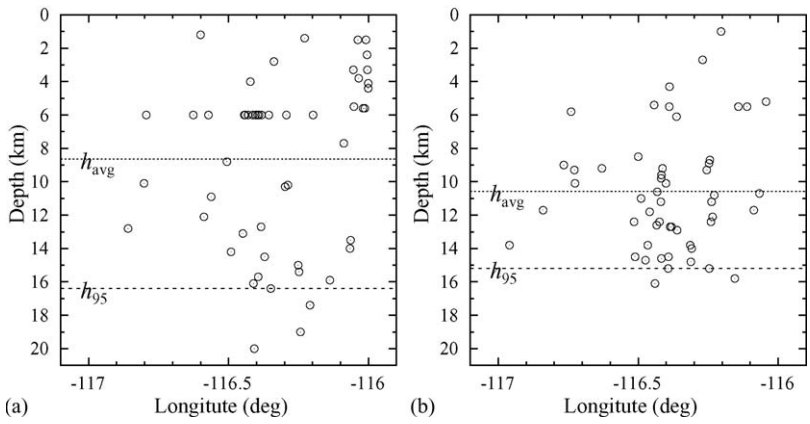

Fig. 8. Focal depth distributions of 52 events with magnitudes larger than 2.3 (a) from 1998 to February 2000 and (b) from March 2000 and 2003. The average depths (h_{avg}) of the two sets are 8.6 and 10.6 km. The depths above which 95% of events are placed (h_{95}) are estimated by 16.4 and 15.2 km.

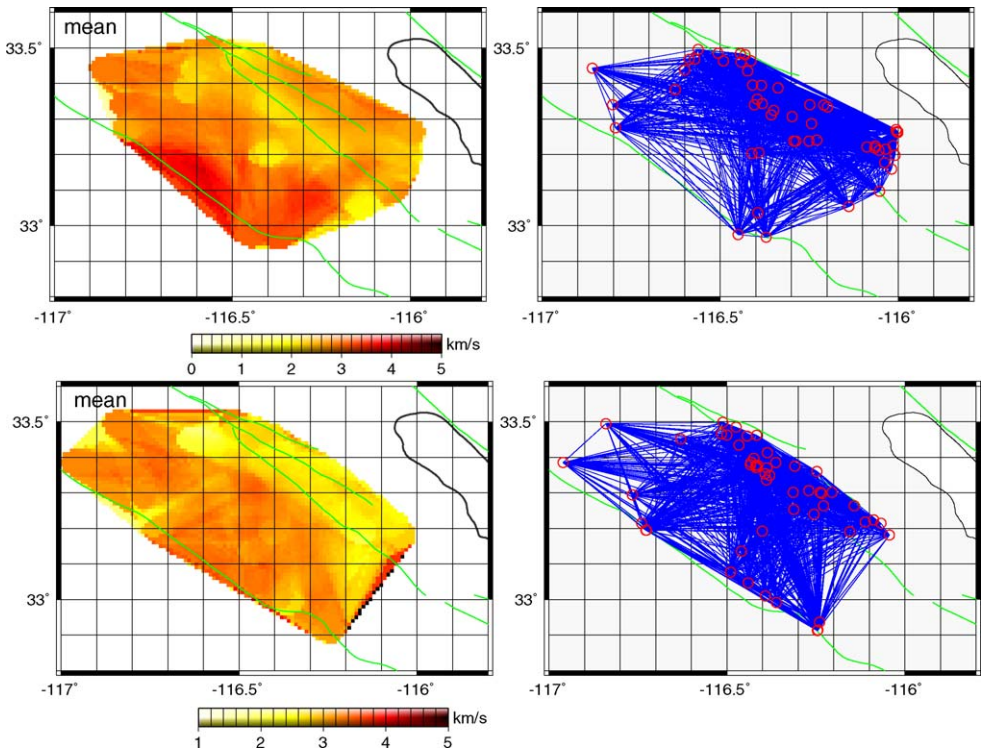

Fig. 9. Tomography results for events of two different time periods (see, Fig. 8). The great-circle paths between events are plotted. The event locations are marked with circles. Different velocity scales are implemented in the tomographic representation for clear display of seismic structures. A low-velocity structure is observed clearly along the San Jacinto fault zone.

the region between the San Jacinto fault zone and the Elsinore fault zone (Perris block) generally increases with depth from 3.2 to 4.4 km/s over the 6 km depth range. This "background" shear velocity is close to the Southern California Earthquake Center (SCEC) crustal model which is based on regional traveltime tomography (Hauksson, 2000; Magistrale et al., 2000; Kohler et al., 2003). The low-velocity regions at the northern and southern ends of the Perris block, at depths of 6–10 km and 13–16 km, agree with Shapiro et al.'s (2005) result, which is based on cross-correlation of noise (see, 7.5 and 15 s period Rayleigh wave results in their Fig. 1).

A low-velocity structure is clearly observed at all depths in the San Jacinto fault zone. In contrast, low-velocity structure is only observed in the northwest portion of the Elsinore fault zone at depths above 10 km. The low velocity structure along the San Jacinto fault zone at depths of 10–13 km is less prominent compared to those at upper and lower depths. Further, the shear velocity of the wear at depths of 10–13 km has higher shear velocity than the depths above and below. Overall, the shear velocity of the San Jacinto fault zone is 10–35% lower than the interior of the Perris block. Also, the shear velocities along the fault trace display a velocity decrease of 6–8% on average to those of immediately adjacent regions. The velocity contrasts are 0.5–0.6 km/s at 10–13 km depth, and 0.6–0.8 km/s at 6–10 km and 13–16 km. We observe several patches with a velocity decrease of around 25% on the San Jacinto fault zone. As we discuss further in the following section, we believe these depth-dependent velocity contrasts of the wear have important tectonic implications.

7. Structural and geological implications

The low-velocity structure in the San Jacinto fault zone extends to a depth of about 16 km, which corresponds to the depth of the brittle–ductile transition zone. This vertical dimension agrees with the results of Li and Vernon (2001) who presents a model with a low-velocity zone extending to 15–20 km depth with a shear velocity contrast with respect to the wall-rock of 25–30%. However, in our model, the seismic velocities of the low-velocity zone do not increase linearly with depth, but instead are separated into upper and lower parts by the low-contrast region described in the previous section. Thus, we expect trapped waves to

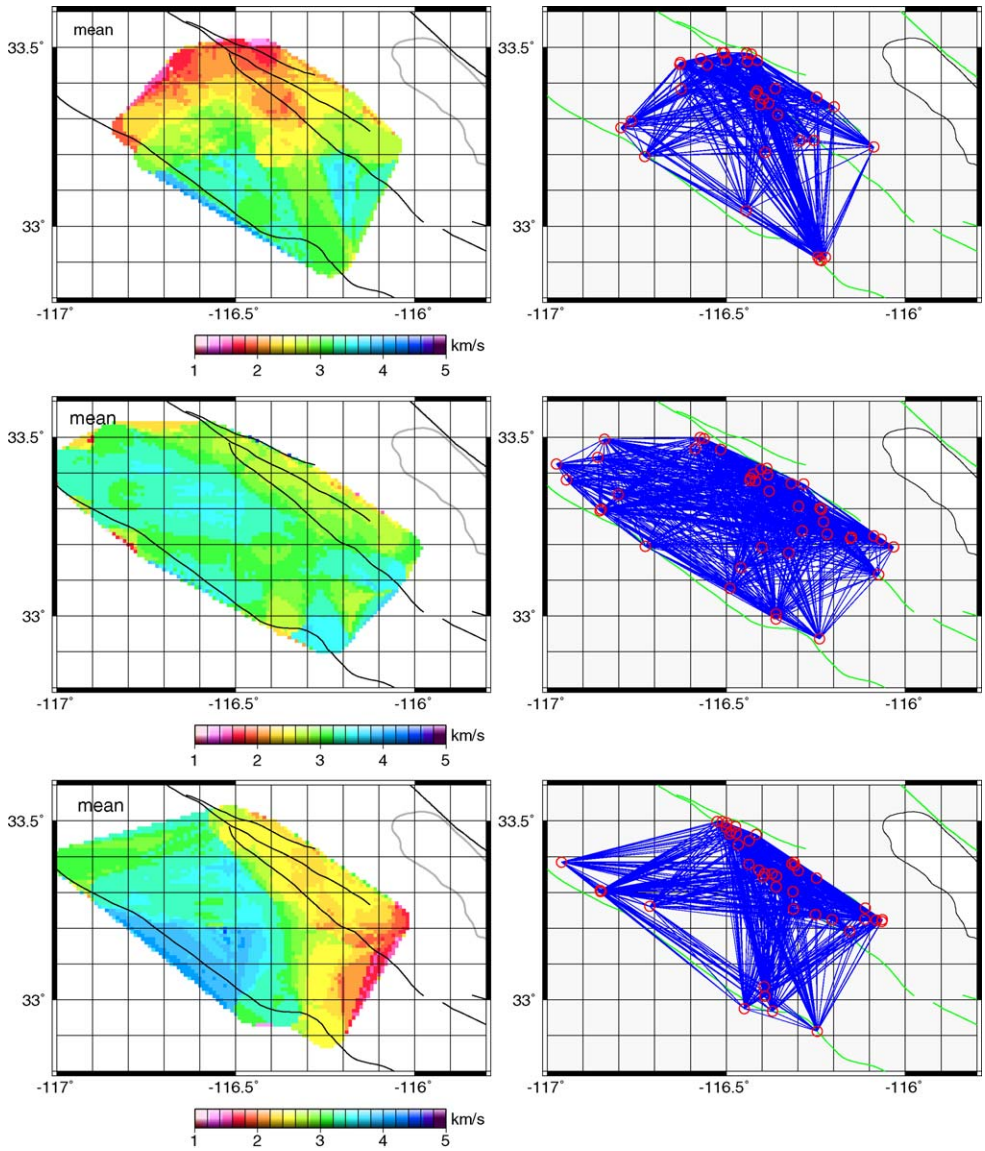

Fig. 10. Shear velocity structures at depths of: (a) 6–10 km; (b) 10–13 km; (c) 13–16 km. The low-velocity structure in the San Jacinto fault zone extends to the base of seismogenic zone.

develop separately in each separate zone. Trapped waves observed on the surface will mainly originate mainly in the shallower low-velocity zone. This result may explain why the model of Lewis et al. (2005), which has a much shallower low-velocity zone, differs from ours.

Many faults in southern California share a common pattern in which stick slip nucleates at a shallow depth (around 5–7 km for the San Andreas fault) and localized large displacement occurs there (Tse and Rice, 1986; Marone and Scholz, 1988). The slip tends to decrease gradually with depth in the middle of the seismogenic zone. At the base of the seismogenic zone, frictional slip increases with depth. The distribution of low velocities with depth, which we observe in the tomographic images, is consistent with this pattern. The high slip rates at shallow and greater depths produce more wear detritus on the fault plane which causes a decrease of seismic velocity in the zones. On the other hand, the diminished slips at the inter-zone perturb the region rather less and the velocity difference with the background medium is reduced.

In quartz-bearing rocks, the transition between unstable rupture and stable steady-state sliding (i.e.,

brittle–ductile transition) occurs at a temperature of 300 °C (Tse and Rice, 1986; Scholz, 1998). In the vicinity of the San Jacinto fault, this transition seems to occur at the substantially-higher temperature of 400° (Bonner et al., 2003). This temperature is high enough for ductile deformation of quartz-bearing rocks, and causes the quartz-rich zone to be an aseismic ductile shear zone which creeps beneath the seismogenic zone with a steady-state slip rate (Scholz, 1998; Shearer, 2002; Ellis and Stockhert, 2004). However, the active seismicity and the low velocity structure imply the presence of strong frictional slip up to a depth of 16 km. The presence of frictional slip in a zone with such high temperature indicates that the dominant constituent materials of the deeper parts of the fault zone (>13 km depth) are probably not quartz-bearing, but rather feldspar-rich rocks such as diabases. The depth of brittle–ductile transition depends on the temperature and the rock composition. The heat flow in the San Jacinto fault zone (80–100 mW/m^2) and the existence of subbasement of diabases at depths beyond 13 km produce a brittle–ductile transition at a depth of 15 km with a possible variation for a couple of kilometers depending on other parameters (Doser and Kanamori, 1986). The slightly deeper (16 km) depth observed in our study region could be explained by variation of other fault-zone properties.

The low-velocity structure in the fault zone is attributed to brittle deformation and its resultant mechanical responses such as fractures, brecciation, fluid saturation and pore pressure, which are accumulated over the geologic time (Li and Vernon, 2001). Considering the maximum shear resistance, excessive frictional slip and the huge shear velocity difference to background medium, materials along the wear-zone boundaries are expected to be melted during the rapid movement of fault. The melted materials appear as glassy fault rocks (pseudotachylite) on the boundaries, and the metamorphism and perturbation in the wear-zone may be reduced with distance from the boundaries.

8. Discussion and conclusions

We have proposed a new imaging technique that uses the principle of spatial reciprocity and cross-correlation to estimate traveltimes between earthquake hypocenters. Our technique is especially useful for studying fault zones, because of the high density of hypocenters there. We have validated the technique through a series of tests and applied it to image the San Jacinto and Elsinore fault zones in southern California.

The low velocity structure in the San Jacinto fault zone is observed consistently down to the depth of the brittle–ductile transition zone, ∼16 km. In contrast, the low velocity structure of the Elsinore fault zone is observed only around the northwest portion at depths shallower than ∼10 km. In the San Jacinto fault, this zone of wear has minimum contrast at depths of 13–16 km. The shear velocity decreases by about 10–35% across the San Jacinto fault zone from west to east. Also, the shear velocities of the wear are lower by around 6–8% than those of the wall-rock.

The active seismicity, high geotherm and the velocity contrast minimum in the wear zone of San Jacinto fault zone imply that the mid-crustal region above the brittle–ductile transition zone is composed of two different materials (sedimentary basement over diabase subbasement). Strong frictional slip is expected at the base of seismogenic zone (13–16 km) in the San Jacinto fault zone.

Acknowledgements

We thank David Schaff for digital fault map of southern California. We also thank Won-Young Kim, Jim Gaherty, Hiroo Kanamori, and Egill Hauksson for fruitful comments. We are grateful to Prof. Brian Kennett and reviewers for the review comments. This is Lamont-Doherty Earth Observatory contribution 6857.

References

Aki, K., Chouet, B., 1975. Origin of coda waves: source, attenuation, and scattering effects. J. Geophys. Res. 80, 3322–3342.

Aki, K., Richards, P.G., 1980. Quantitative Seismology, Theory and Methods, vol. 1. W.H. Freeman and Company, San Francisco.

Bonner, J.L., Blackwell, D.D., Herrin, E.T., 2003. Thermal constraints on earthquake depths in California. Bull. Seism. Soc. Am. 93, 2333–2354.

Campillo, M., Paul, A., 2003. Long-range correlations in the diffuse seismic coda. Science 299, 547–549.

Doser, D.I., Kanamori, H., 1986. Depth of Seismicity in the Imperial-Valley region (1977–1983) and its relationship to heat-flow, crustal structure, and the October 15, 1979, earthquake. J. Geophys. Res. 91 (B1), 675–688.

Ellis, S., Stockhert, B., 2004. Elevated stresses and creep rates beneath the brittle–ductile transition caused by seismic faulting in the upper crust. J. Geophys. Res. 109, B05407, doi:10.1029/2003JB002744.

Grant, L.B., Shearer, P.M., 2004. Activity of the offshore NewPort-Inglewood Rose Canyon fault zone, costal southern California, from relocated micro-seismicity. Bull. Seism. Soc. Am. 94 (2), 747–752.

Hauksson, E., 2000. Crustal structure and seismicity distribution adjacent to the Pacific and North America plate boundary in southern California. J. Geophys. Res. 105 (B6), 13,875–13,903.

Hauksson, E., Shearer, P., 2005. Southern California hypocenter relocation with waveform cross-correlation, part 1: results, using the

double-difference method. Bull. Seism. Soc. Am. 95 (3), 896–903.

Hong, T.-K., 2004. Scattering attenuation ratios of P and S waves in elastic media. Geophys. J. Int. 158 (1), 211–224.

Hong, T.-K., Kennett, B.L.N., 2003. Modelling of seismic waves in heterogeneous media using a wavelet-based method: application to fault and sub-duction zones. Geophys. J. Int. 154, 483–498.

Hong, T.-K., Menke, W., submitted for publication. Imaging laterally-varying regional crustal heterogeneities from seismic coda of single-station records for clustered events, Geophys. J. Int.

Hong, T.-K., Xie, J., 2005. Phase composition of regional seismic waves from underground nuclear explosions. J. Geophys. Res. 110, B12302, doi:10.1029/2005JB003753.

Kennedy, M.P., Morton, D.M., 2003. Preliminary geologic map of the Murrieta 7.5′ quadrangle, Riverside County, California, U.S. Geological Survey, Open-File Report 03-189.

Kohler, M.D., Magistrale, H., Clayton, R.W., 2003. Mantle heterogeneities and the SCEC reference three-dimensional seismic velocity model version 3. Bull. Seism. Soc. Am. 93 (2), 757–774.

Jennings, C.W., 1994. Fault Activity Map of California and Adjacent Areas with Location and Ages of Recent Volcanic Eruptions, California Geologic Data Map Series, Map No. 6. California Division of Mines and Geology.

Lewis, M.A., Peng, Z., Ben-Zion, Y., Vernon, F.L., 2005. Shallow seismic trapping structure in the San Jacinto fault zone near Anza, California. Geophys. J. Int. 162, 867–881.

Li, Y.-G., Aki, K., Vernon, F.L., 1997. San Jacinto fault zone guided waves: a discrimination for recently active fault strands near Anza, California. J. Geophys. Res. 102 (B6), 11,689–11,701.

Li, Y.-G., Vernon, F.L., 2001. Characterization of the San Jacinto fault zone near Anza, California, by fault zone trapped waves. J. Geophys. Res. 106 (B12), 30,671–30,688.

Li, Y.-G., Vidale, J.E., Day, S.M., Oglesby, D.D., the SCEC Field Working Team, 2002. Study of the 1999 M7.1 Hector Mine, California, earthquake fault plane by trapped waves. Bull. Seism. Soc. Am. 92 (4), 1318–1332.

Magistrale, H., 2002. Relative contributions of crustal temperature and composition to controlling the depth of earthquakes in southern California. Geo-phys. Res. Lett. 29 (10), 1447, doi:10.1029/2001GL014375.

Magistrale, H., Day, S., Clayton, R.W., Graves, R., 2000. The SCEC southern California reference three-dimensional seismic velocity model version 2. Bull. Seism. Soc. Am. 90, S65–S76.

Magistrale, H., Rockwell, T., 1996. The central and southern Elsinore fault zone, southern California. Bull. Seism. Soc. Am. 86 (6), 1793–1803.

Marone, C., Scholz, C.H., 1988. The depth of seismic faulting and the upper transition from stable to unstable slip regimes. Geophys. Res. Lett. 15 (6), 621–624.

Mizuno, T., Nishigami, K., Ito, H., Kuwahara, Y., 2004. Deep structure of the Mozumi-Sukenobu fault, central Japan, estimated from the subsurface array observation of fault zone trapped waves. Geophys. J. Int. 159, 622–642.

Nazareth, J.J., Hauksson, E., 2004. The seismogenic thickness of the southern California crust. Bull. Seism. Soc. Am. 94 (3), 940–960.

Nowack, R., Chen, W.-P., 1999. Source-receiver reciprocity and empirical Green's functions from chemical blasts. Bull. Seism. Soc. Am. 89, 538–543.

Paul, A., Campillo, M., Margerin, L., Larose, E., Derode, A., 2005. Empirical synthesis of time-asymmetrical Green functions from the correlation of coda waves. J. Geophys. Res. 110, B08302, doi:10.1029/2004JB003521.

Rolandone, F., Biirgmann, R., Nadeau, R.M., 2004. The evolution of the seismic-aseismic transition during the earthquake cycle: constraints from the time-dependent depth distribution of aftershocks. Geophys. Res. Lett. 31, L23610, doi:10.1029/2004GL021379.

Sanders, C.O., Kanamori, H., 1984. A seismotectonic analysis of the Anza seismic gap, San Jacinto Fault Zone, southern California. J. Geophys. Res. 89 (B7), 5873–5890.

Scherbaum, F., Gilard, D., Deichmann, N., 1991. Slowness power analysis of the coda composition of two microearthquake clusters in northern Switzerland. Phys. Earth Planet. Inter. 67, 137–161.

Scholz, C.H., 1998. Earthquakes and friction laws. Nature 391, 37–42.

Scott, J.S., Masters, T.G., Vernon, F.L., 1994. 3-D velocity structure of the San Jacinto fault zone near Anza, California-I. P waves. Geophys. J. Int. 119, 611–626.

Shapiro, N.M., Campillo, M., 2004. Emergence of broadband Rayleigh waves from correlations of the ambient seismic noise. Geophys. Res. Lett. 31, L07614, doi:10.1029/2004GL019491.

Shapiro, N.M., Campillo, M., Stehly, L., Ritzwoller, M.H., 2005. High resolution surface wave tomography from ambient seismic noise. Science 307, 1615–1618.

Shearer, P.M., 2002. Parallel fault strands at 9-km depth resolved on the Imperial Fault, southern California. Geophys. Res. Lett. 29 (14), 1674, doi:10.1029/2002GL015302.

Sibson, R.H., 1984. Roughness at the base of the seismogenic zone: contributing factors. J. Geophys. Res. 89 (B7), 5791–5799.

Snieder, R., 2004. Extracting the Green's function from the correlation of coda waves: a derivation based on stationary phase. Phys. Rev. E. 69, 046610, doi:10.1103/PhysRevE.66.046610.

Spudich, P., Bostwick, T., 1987. Studies of the seismic coda using an earthquake cluster as a deeply buried seismograph array. J. Geophys. Res. 92 (B10), 10,526–10,546.

Tse, S.T., Rice, J.R., 1986. Crustal earthquake instability in relation to the depth variation of frictional slip properties. J. Geophys. Res. 91 (B9), 9452–9472.

Walls, C., Rockwell, T., Mueller, K., Bock, Y., Williams, S., Pfanner, J., Dolan, J., Feng, P., 1998. Escape tectonics in the Los Angeles meteropoli-tan region and implications for seismic risk. Nature 394, 356–360.

Xie, J., Cong, L., Mitchell, B.J., Chiu, J.-M., 1996. Complexities in high-frequency seismic waveforms due to three-dimensional structure in the New Madrid Seismic Zone. J. Geophys. Res. 101 (B3), 5751–5778.